The Astrophysical Journal, 978:123 (9pp), 2025 January 10 https://doi.org/10.3847/1538-4357/ad95f5

CO Observations of the Type Ia Supernova Remnant 3C 397 by the Nobeyama 45 m Radio Telescope: Possible Evidence for the Single-degenerated Explosion

D. Ito[1,2], H. Sano[2,3], K. Nakazawa[4], I. Mitsuishi[1], Y. Fukui[1], H. Sudou[2,5], and H. Takaba[2]
[1] Department of Physics, Nagoya University, Furo-cho, Chikusa-ku, Nagoya 464-8601, Japan; ito_d@u.phys.nagoya-u.ac.jp
[2] Faculty of Engineering, Gifu University, 1-1 Yanagido, Gifu 501-1193, Japan; sano.hidetoshi.w4@f.gifu-u.ac.jp
[3] Center for Space Research and Utilization Promotion (c-SRUP), Gifu University, 1-1 Yanagido, Gifu 501-1193, Japan
[4] Kobayashi-Maskawa Institute for the Origin of Particles and the Universe, Nagoya University, Nagoya-shi, Aichi, Japan
[5] National Institute of Technology, Sendai College 48 Nodayama, Medeshima-Shiote, Natori, Miyagi 981-1239, Japan
Received 2024 February 22; revised 2024 November 19; accepted 2024 November 20; published 2024 December 31

Abstract

We present a new CO observation toward the Type Ia supernova remnant 3C 397 using the Nobeyama 45 m radio telescope at an unprecedented angular resolution of $\sim 18''$. We newly found that the CO cloud at $V_{\rm LSR} = 55.7$–$62.2\,{\rm km\,s^{-1}}$ ($60\,{\rm km\,s^{-1}}$ cloud) shows a good spatial correspondence with the radio continuum shell. We also found an expanding gas motion of the $60\,{\rm km\,s^{-1}}$ cloud with an expansion velocity of $\sim 3\,{\rm km\,s^{-1}}$, which is thought to be formed by the pre- and/or postsupernova feedback. By considering the positions of Galactic spiral arms and the X-ray/H I absorption studies, we concluded that 3C 397 is physically associated with the $60\,{\rm km\,s^{-1}}$ cloud rather than the previously known CO cloud at $V_{\rm LSR} \sim 30\,{\rm km\,s^{-1}}$. Given that the previously measured preshock density is $\sim$2–5 ${\rm cm^{-3}}$, the expanding motion of the $60\,{\rm km\,s^{-1}}$ cloud was likely formed by the presupernova feedback known as optically thick wind. The scenario is consistent with the fact that 3C 397 exploded inside a wind-blown bubble as a single degenerate system.

Unified Astronomy Thesaurus concepts: Supernova remnants (1667); Interstellar medium (847); X-ray sources (1822)

1. Introduction

Identifying progenitor systems of Type Ia supernovae (SNe) is a pressing issue in modern astrophysics. This is because it is the standard candle in the Universe due to its constant absolute luminosity (e.g., I. P. Pskovskii 1977; M. M. Phillips 1993; M. M. Phillips et al. 1999). "Single-degenerate (SD)" and "double-degenerate (DD)" are the two most widely accepted scenarios to describe the progenitor systems of Type Ia SNe. The SD scenario is the accretion of gas from a companion star onto a white dwarf, reaching the Chandrasekhar limit, and an ensuing thermonuclear explosion (e.g., J. Whelan & I. J. Iben 1973; K. Nomoto 1982; K. Nomoto et al. 1984). On the other hand, the DD scenario is an explosion caused by merging two white dwarfs (e.g., R. F. Webbink 1984; I. Iben & A. V. Tutukov 1984). Only for the SD scenario, there exists a companion star blown away by the explosion, so it is the simplest evidence to identify the companion star. However, there is no strong case of observational identification of the companion star, although many studies have been performed (e.g., D. Maoz et al. 2014; K. Maeda & Y. Terada 2016).

An alternative way to verify the SD scenario is to find an expanding shell interacting with a Type Ia supernova remnant (SNR). Because the expanding gaseous shell surrounding a Type Ia SNR could be formed by disk winds, referred to as "optically thick wind (OTW)," from the progenitor of a binary system comprising a white dwarf and a nondegenerate companion (e.g., I. Hachisu et al. 1996, 1999a, 2000). When the mass accretion rate of the interstellar medium from the companion to the white dwarf exceeds a critical value, strong winds blow to stabilize mass transfer, forming a low-density bubble, and then the SN explosion occurs in it (C. Badenes et al. 2007). The shell size formed by the OTW depends not only on the accretion wind parameters but also on the gas density of the surrounding medium (B.-C. Koo & C. F. McKee 1992a, 1992b). A series of processes are observed only in the SD scenario, but not in the DD scenario.

Such attempts to explain SD scenarios in terms of an expanding shell have been performed in previous studies. The first detection of an expanding shell was the ^{12}CO observation of SN 1572 (P. Zhou et al. 2016). They found an expanding shell with mass $\sim 220\,M_{\odot}$ and expansion velocity $\Delta V \sim 5\,{\rm km\,s^{-1}}$ and argued that its momentum is sufficiently explained by energy injection from the OTW. They concluded that SN 1572 was produced by the SD scenario. Other Type Ia SNRs such as N103B, G344.7−0.1, and SN 1006 also showed expanding shells possibly due to the OTW (H. Sano et al. 2018, 2022; K. Fukushima et al. 2020). To explain the progenitor systems of Type Ia SNe in the SD scenario, further CO observations in other Type Ia SNRs are needed to test the scenario.

3C 397 (G41.1−0.3) is a bright Type Ia SNR in X-ray and radio wavelengths at $(l, b) \sim (41.^{\circ}1, -0.^{\circ}3)$. The SNR is classified as a mixed-morphology type whose central region is bright in thermal X-rays and distributed on a shell in radio continuum emission, which shows a rectangular shell elongated in the east–west direction with an apparent size of $4.'5 \times 2.'5$ (e.g., R. H. Becker et al. 1985; M. C. Anderson & L. Rudnick 1993; J. Rho & R. Petre 1998; S. Safi-Harb et al. 2005). The age discrepancies are $\sim$1350−1500 yr for radio (D. A. Leahy & S. Ranasinghe 2016) and $\sim$5000 yr for X-ray observations (S. Safi-Harb et al. 2005).

3C 397 has been observed in radio, infrared, X-ray, and gamma rays (e.g., S. Safi-Harb et al. 2000; B. Jiang et al. 2010;

H. Yamaguchi et al. 2015; Y.-H. Lee et al. 2019; T. Ergin et al. 2021; Y. Ohshiro et al. 2021). Y.-H. Lee et al. (2019) concluded that the SNR morphology is not due to an asymmetric explosion but to an explosion within an inhomogeneous interstellar medium based on near-infrared [Fe II] emission and radio continuum observations. H. Yamaguchi et al. (2015) detected K-shell emission lines from Cr, Mn, Fe, and Ni using Suzaku that cannot be explained without electron capture during explosions and found that their mass ratios of Mn/Fe and Ni/Fe are very high, suggesting that 3C 397 has a progenitor of the SD scenario.

3C 397 is thought to be associated with the dense molecular clouds by radio-line observations. S. Safi-Harb et al. (2005) carried out CO($J = 2$–1) and CO($J = 1$–0) observations with the Swedish-ESO Submillimeter Telescope and the Mopra telescope, which have angular resolutions of $\sim$22″ and $\sim$45″, respectively. The authors found that the molecular clouds at a velocity of $\sim$38−40 km s^{-1} are well spatially correlated with the X-ray brightness on the western shell of the SNR. Subsequent ^{12}CO($J = 1$–0) observations using the 13.7 m telescope at the Purple Mountain Observatory suggested the cloud association at the velocity range of $\sim$27−35 km s^{-1}, except for the southeastern shell of the SNR (B. Jiang et al. 2010). The authors also found possible evidence for a line-broadening of CO at a velocity of $\sim$32 km s^{-1}.[6] Both authors estimated the kinematic distance of the clouds to be $\sim$10 kpc, which is consistent with a large absorbing column density of X-rays. On the other hand, there are no detailed CO studies that focus on the other velocity components and kinematics of the gas, e.g., an expanding motion of the clouds. Moreover, the 1420 MHz H I absorption studies suggested that the systemic velocity of 3C 397 is $\sim$50–60 km s^{-1}, corresponding to the lower and upper limits of kinematic distances to be 6.3 ± 0.1 and 9.7 ± 0.3 kpc, respectively (D. A. Leahy & S. Ranasinghe 2016). If this is correct, the shock-interacting molecular clouds with 3C 397 would need to be reconsidered.

In the present paper, we report new millimeter-wavelength observations using ^{12}CO($J = 1$–0) line emission with the Nobeyama 45 m radio telescope (NRO45) and archival ^{12}CO($J = 3$–2) data using the James Clerk Maxwell Telescope (JCMT). The CO data sets with unprecedented sensitivity and high angular resolution of $\sim$20″ enable us to identify interacting molecular clouds and their physical relation to the high-energy phenomena in 3C 397. Section 2 describes the observational data sets and their reductions. Section 3 comprises three subsections: Sections 3.1 and 3.2 present overviews of the distributions of X-rays, the radio continuum, and CO, and Section 3.3 shows the X-ray hardness ratio (HR). A discussion and conclusions are given in Sections 4 and 5, respectively.

2. Observations and Data Reduction

2.1. CO

We performed ^{12}CO($J = 1$–0) observations at 115.271202 GHz with NRO45 on 2022 December 7, (proposal No. G22030, PI: H. Sano). We used the on-the-fly mapping mode for a 12′ × 12′ rectangular region centered at (l, b) = (41.°12, −0.°31). The front end was the FOur-beam REceiver System on a 45 m Telescope (FOREST; T. Minamidani et al. 2016), a dual-polarization, double sideband, four-beam heterodyne receiver with a superconductor-insulator-superconductor mixer driven at 80–116 GHz. The back end was an FX-type digital spectrograph named Spectral Analysis Machine for 45 m Telescope (SAM45; N. Kuno et al. 2011). The bandwidth was 125 MHz, and the channel width was 61.04 kHz in the spectral window mode. The typical system temperature was $\sim$340 K for both V and H polarization including the atmosphere. The final beam size was $\sim$18′ in the full-width half-maximum (FWHM). The pointing accuracy was achieved to be better than $\sim$2′ through hourly observations of the SiO maser OH39.7 +1.5. We also observed W51[(α_{B1950}, δ_{B1950}) = ($19^h21^m26.^s2$, 14°24′43.″0)] for the absolute intensity calibration, and then we estimated the extended main beam efficiency of $\sim$0.56 through a comparison with the archival FUGIN data (T. Umemoto et al. 2017). The final data has a noise fluctuation of $\sim$0.11 K at the velocity resolution of 0.65 km s^{-1}.

We also used archival data of ^{12}CO($J = 3$–2) line emission at 345.795990 GHz observed with JCMT by the ^{12}CO($J = 3$–2) High-Resolution Survey (COHRS DR2; G. Park et al. 2023). The angular resolution is $\sim$16.″6 in the FWHM. We applied the main beam efficiency of $\sim$0.61 to convert the data from antenna temperature T_a^* to main-beam temperature T_{mb} (G. Park et al. 2023). The final data has a noise fluctuation of $\sim$0.11 K at the velocity resolution of 0.65 km s^{-1}.

2.2. Radio Continuum

To compare CO distributions with the SNR shell morphology, we used the 20 cm radio continuum data taken with the Very Large Array (VLA) as a part of the Multi-Array Galactic Plane Imaging Survey (D. J. Helfand et al. 2006). The angular resolution is 6.″4 × 5.″4 with a position angle of 350°, and the typical noise fluctuation is $\sim$0.3 mJy beam^{-1}.

2.3. X-Rays

We used archival X-ray data obtained by Chandra with the ACIS-I array (Obs ID: 1042), which has been published by several papers (e.g., S. Safi-Harb et al. 2005; B. Jiang et al. 2010; B.-C. Koo et al. 2016). We used CIAO version 4.14 (A. Fruscione et al. 2006) with CALDB 4.9.4 (D. Graessle et al. 2006) for data reduction and imaging. After reprocessing all data using the `chandra_repro` procedure, we created energy-filtered, exposure-corrected maps using the `flux_image` procedure in the energy bands of 0.5–7.0 keV (broad band), 1.14–1.27 keV (soft band), and 3.3–3.7 keV (hard band). The effective exposure time was $\sim$66 ks. We smoothed each image to improve the signal-to-noise ratio: the final beam size of the soft and medium band images is to be $\sim$10″ and that of the broadband image is $\sim$3″ in the FWHM.

3. Results

3.1. Overview of X-Ray and Radio Continuum

Figure 1 shows the Chandra X-ray image at 0.5–0.7 keV superposed on the VLA radio continuum contours at 1.4 GHz. As presented in previous studies, X-rays are concentrated in the center of the SNR and show the elongated distribution in the east–west direction (e.g., J. Rho & R. Petre 1998). The radio continuum shows enhancement in the southeast and southwest, consistent with an X-ray distribution brighter than $\sim 5 \times 10^{-6}$ photons cm^{-2} s^{-1}. Similarly, in the northeastern part of the SNR, there is an area of slightly higher intensity in X-rays

[6] This line-broadening is also mentioned by C. D. Kilpatrick et al. (2016) using the Heinrich Submillimeter Telescope.

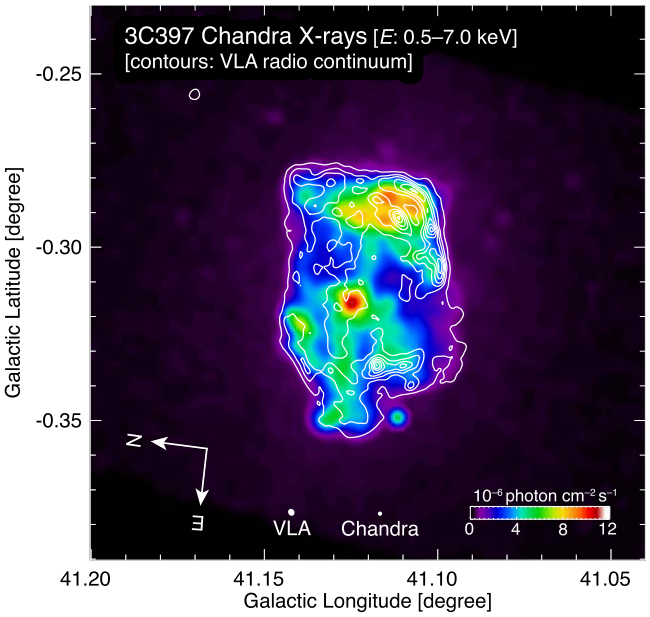

Figure 1. Distribution of Chandra X-ray intensity (*E*: 0.5–7.0 keV; e.g., S. Safi-Harb et al. 2005) superposed on the VLA radio continuum at 1.4 GHz (D. J. Helfand et al. 2006). The lowest contour level and intervals are 1.5 and 7.5 mJy beam^{-1}, respectively.

($\sim 7 \times 10^{-6}$ photons cm^{-2} s^{-1}), corresponding to the distribution of the radio shell. No significant enhancement of radio emission was observed in the northwest direction. The intensity distributions of both the radio and X-rays extend east to west from the center of the SNR, which were mentioned as "jet-like structures" by S. Safi-Harb et al. (2005).

3.2. Distributions of CO Clouds

Figure 2 shows the velocity channel maps of ^{12}CO($J = 1$–0) toward 3C 397 for two velocity ranges of 27.1–36.8 km s^{-1} (hereafter the "30 km s^{-1} cloud") and 55.7–62.2 km s^{-1} (hereafter the "60 km s^{-1} cloud"). The 30 km s^{-1} cloud is believed to be associated with the SNR (S. Safi-Harb et al. 2005; B. Jiang et al. 2010), while the 60 km s^{-1} cloud represents the systemic velocity of 3C 397 by the H I absorption study (D. A. Leahy & S. Ranasinghe 2016).

In the 30 km s^{-1} cloud (Figure 2 upper panels), ^{12}CO emission partially surrounds the northern and western boundaries of the radio shell in the velocity range of 29.00–32.9 km s^{-1}. On the other hand, the ^{12}CO cloud at the velocity range of 34.9–36.8 km s^{-1} is almost filled inside the radio shell. In the 60 km s^{-1} cloud (Figure 2 lower panels), we also found that clumpy and diffuse molecular clouds are distributed along the northern half of the radio shell. We also noted that a filamentary CO cloud elongated east and west from the center of the SNR ($V_{\rm LSR}$: 55.7–58.3 km s^{-1}) seems to overlap with the jet-like structure of the radio continuum and X-rays (see Figure 1).

Figures 3(a) and (b) show the velocity-integrated intensity maps of ^{12}CO($J = 1$–0) for the 30 and 60 km s^{-1} clouds, respectively. The 30 km s^{-1} cloud extends the western half of the SNR shell, while the 60 km s^{-1} cloud mainly lies on the northern half of the SNR. We also find clumpy ^{12}CO($J = 3$–2) clouds in the 60 km s^{-1} cloud, some of which are along the radio shell boundary.

Figures 3(c) and (d) show enlarged maps of the northwestern and southwestern parts of the SNR using the JCMT ^{12}CO($J = 3$–2) line data. The velocity range is 59.6–60.0 km s^{-1} for Figure 3(c) and 57.0–58.3 km s^{-1} for Figure 3(d). Both the molecular clouds are nicely along the radio-bright edge or shell. Particularly, the dogleg shape of the northwestern radio shell is perfectly along the clumpy cloud distribution.

Figures 4(a) and (b) show the position–velocity for the two molecular clouds. The 30 km s^{-1} cloud shows no apparent distribution, which corresponds to the spatial extent of the SNR. On the other hand, the 60 km s^{-1} cloud shows a cavity-like distribution in the *p*–*v* diagram of ^{12}CO emission, whose velocity range is from 56 to 62 km s^{-1}. It is noteworthy that the spatial extent of the cavity is roughly consistent with the diameter of the SNR.

3.3. Comparison with an X-Ray HR

In order to clarify a distance relation between the molecular clouds in the line-of-sight direction of 3C 397, we examined the HR of the X-ray. HR is the ratio of X-ray intensities defined as

$$\mathrm{HR} = \frac{F_{\rm high} - F_{\rm low}}{F_{\rm high} + F_{\rm low}}, \quad (1)$$

where $F_{\rm high}$ is the intensity of X-ray in the high energy band and $F_{\rm low}$ is that of the low energy band. Since the soft-band X-rays should be absorbed by dust grains inside a molecular cloud via photoelectric absorption, we can expect a large HR value when dense molecular clouds are located between the SNR and observers in the line-of-sight direction. So, we searched the dense molecular clouds, which are spatially corresponding to the larger value of HR.

Figure 5 shows the HR images superposed on the ^{12}CO($J = 1$–0) contours for three different velocity ranges. We found three regions of relatively high HR. These coordinates are (l, b) $\sim$ (41.°13, $-0.°28$), (41.°14, $-0.°31$), and (41.°11, $-0.°31$), defined in the order as peak A, peak B, and peak C. The dense molecular cloud (hereafter referred to as "abs cloud" in Figure 5(c)) shows that the abs cloud aligns well with all HR peaks, whereas the 30 km s^{-1} cloud aligns only with peaks A and B, and the 60 km s^{-1} cloud with peak B alone. No other molecular clouds with good spatial counterparts other than these in the other velocity ranges are found.

4. Discussion

4.1. Molecular Clouds Associated with 3C 397

Previous studies proposed that the 30 km s^{-1} cloud is physically interacting with the SNR 3C 397 (e.g., S. Safi-Harb et al. 2005; B. Jiang et al. 2010; C. D. Kilpatrick et al. 2016). Their argument is based on three observational signatures: (1) the bow-shaped spatial distribution of ^{12}CO($J = 1$–0), (2) the line broadening of $\sim$7 km s^{-1} in the ^{12}CO($J = 1$–0) spectrum, and (3) the density of molecular gas assuming a pressure balance between hot and cold gas. In this section, we discuss which of the two clouds, the 30 km s^{-1} cloud and the newly found 60 km s^{-1} cloud, is associated with 3C 397 in terms of spatial/velocity distributions and the positional relation among the molecular clouds and 3C 397 toward the line of sight.

First, we emphasize that it is very difficult to clarify which clouds are physically associated with 3C 397 in terms of spatial comparison alone. Both the 30 and 60 km s^{-1} clouds show good spatial correspondence with the radio continuum shell of

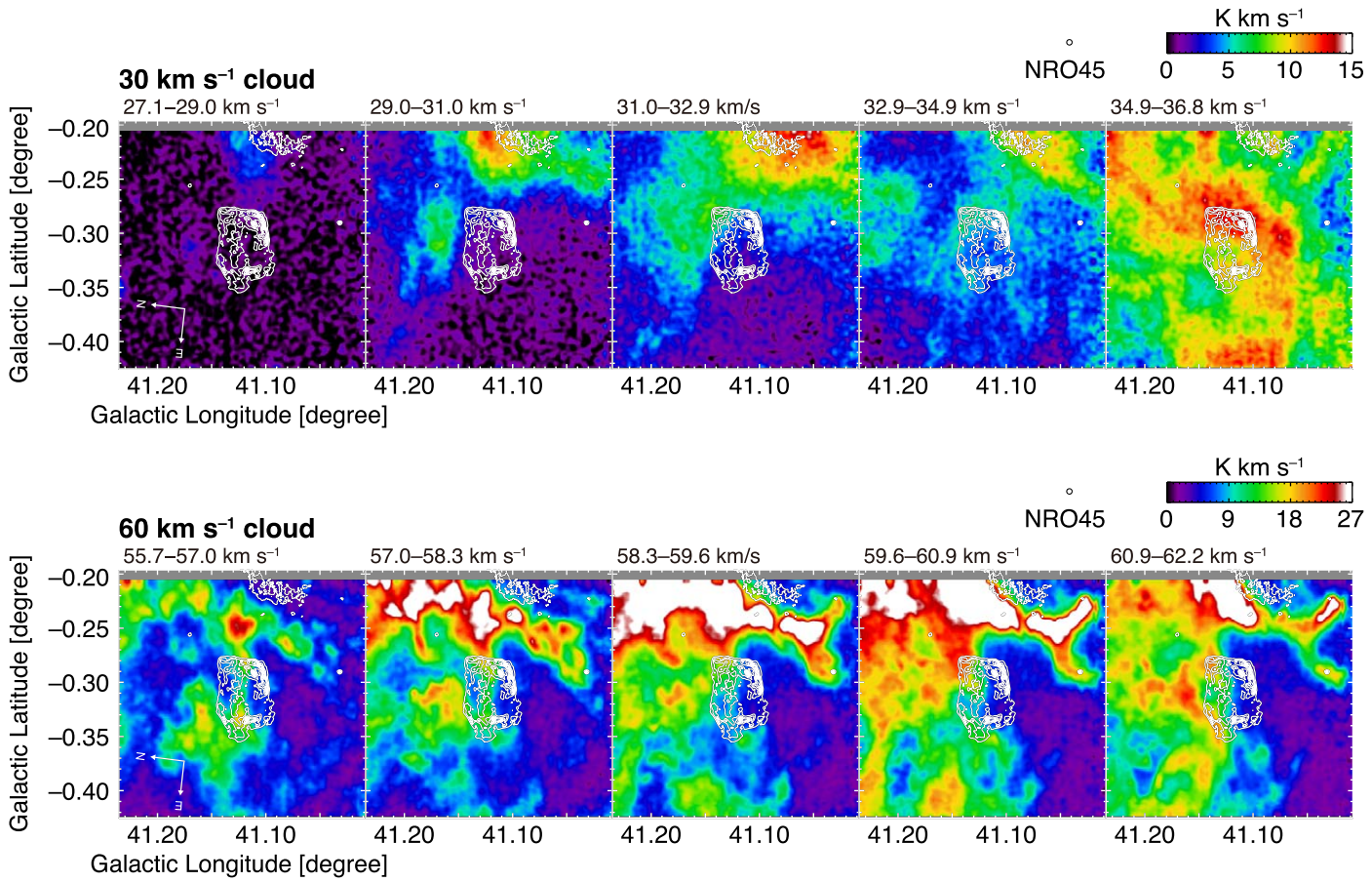

Figure 2. Velocity channel distributions of the NRO45 ^{12}CO($J = 1$–0) for the 30 km s^{-1} cloud (upper panels) and the 60 km s^{-1} cloud (lower panels). Each panel shows the CO integrated intensity distribution integrated over the velocity range of 27.1–36.8 km s^{-1} every 1.95 km s^{-1} for the 30 km s^{-1} cloud and 55.7–62.2 km s^{-1} every 1.3 km s^{-1} for the 60 km s^{-1} cloud. The superposed contours are the same as those shown in Figure 1.

3C 397. The diffuse gas of the 30 km s^{-1} cloud appears to be along the western half of the shell. The ^{12}CO($J = 3$–2) clumpy structure in the 60 km s^{-1} cloud is located in the vicinity of the nonthermal radio-bright shell, indicating that the shock–cloud interaction with magnetic field amplification occurred (e.g., T. Inoue et al. 2009, 2012; H. Sano et al. 2010, 2013).

Next, we argue that the cavity-like structure in the p–v diagram of the 60 km s^{-1} cloud represents an expanding gas motion due to the pre- and/or postsupernova feedback effect. The presupernova feedback corresponds to strong winds from the massive progenitor or OTW from a binary star system including a white dwarf (e.g., R. Weaver et al. 1977; I. Hachisu et al. 1996, 1999a, 1999b). The postsupernova feedback represents the gas acceleration and/or distraction of SN shocks (e.g., B.-C. Koo et al. 1990; M. Seta et al. 1998, 2004). In the case of 3C 397, the expansion velocity of the gas was estimated to be $\Delta V \sim 3$ km s^{-1} centered at the systemic velocity of $\sim 59 \pm 2$ km s^{-1}. The derived expansion velocity is roughly consistent with those of the Galactic SNR SN 1006 (e.g., $\Delta V \sim 4$ km s^{-1}; H. Sano et al. 2022), G344.7−0.1 (e.g., $\Delta V \sim 4.5$ km s^{-1}; K. Fukushima et al. 2020), and G298.6−0.0 (e.g., $\Delta V \sim 8$ km s^{-1}; P. K. H. Yeung et al. 2023). On the other hand, the p–v diagram of the 30 km s^{-1} cloud does not show such an apparent signature of an expanding gas motion.

Finally, we discuss the positional relation among the 30 km s^{-1} cloud, 60 km s^{-1} cloud, abs cloud ($V_{\rm LSR}$: 63.5–64.8 km s^{-1}), and 3C 397 toward the line-of-sight direction, in order to check consistency with observational signature, especially in the HR image. We first examined the velocity distribution of the gas in the line-of-sight direction based on the spiral arm distribution. Figure 6 shows the large-scale p–v diagram of the ^{12}CO($J = 1$–0) obtained using the NANTEN 4 m radio telescope (A. Mizuno & Y. Fukui 2004). According to M. J. Reid et al. (2016) the Sagittarius arm, one of the Galactic spiral arms, lies on the line-of-sight direction of 3C 397, whose systemic velocities are ∼35 km s^{-1} (nearside arm) and ∼60 km s^{-1} (farside arm). This implies that the three molecular clouds discussed in this paper are likely on the Sagittarius arm, and their locations are naturally limited to the nearside arm for the 30 km s^{-1} cloud, and the farside arm for the 60 km s^{-1} cloud and abs cloud. Based on the Galactic rotation model by J. Brand & L. Blitz (1993), the kinematic distance is estimated to be ∼2.1 kpc for the 30 km s^{-1} cloud, ∼8.3 kpc for the abs cloud, and ∼8.7 ± 0.2 kpc for the 60 km s^{-1} cloud (see Figure 7). From the above discussion, the positional relation among the molecular clouds and 3C 397 in the line-of-sight direction should be expressed as schematically shown in Figure 8. This picture is consistent with the HR study as shown in Section 3.3: the abs cloud is located in front of the SNR because peak C of HR is only spatially correlated with the abs cloud. We emphasized that the positional relation is also consistent with the previous H I absorption measurement because the absorption line is seen up to the tangent velocity and absence of absorption at $V_{\rm LSR} = 50$–60 km s^{-1} (D. A. Leahy & S. Ranasinghe 2016).

To summarize the above discussion, we conclude that 3C 397 is likely associated with the 60 km s^{-1} cloud in terms of spatial/velocity distributions of gas (including the previous H I

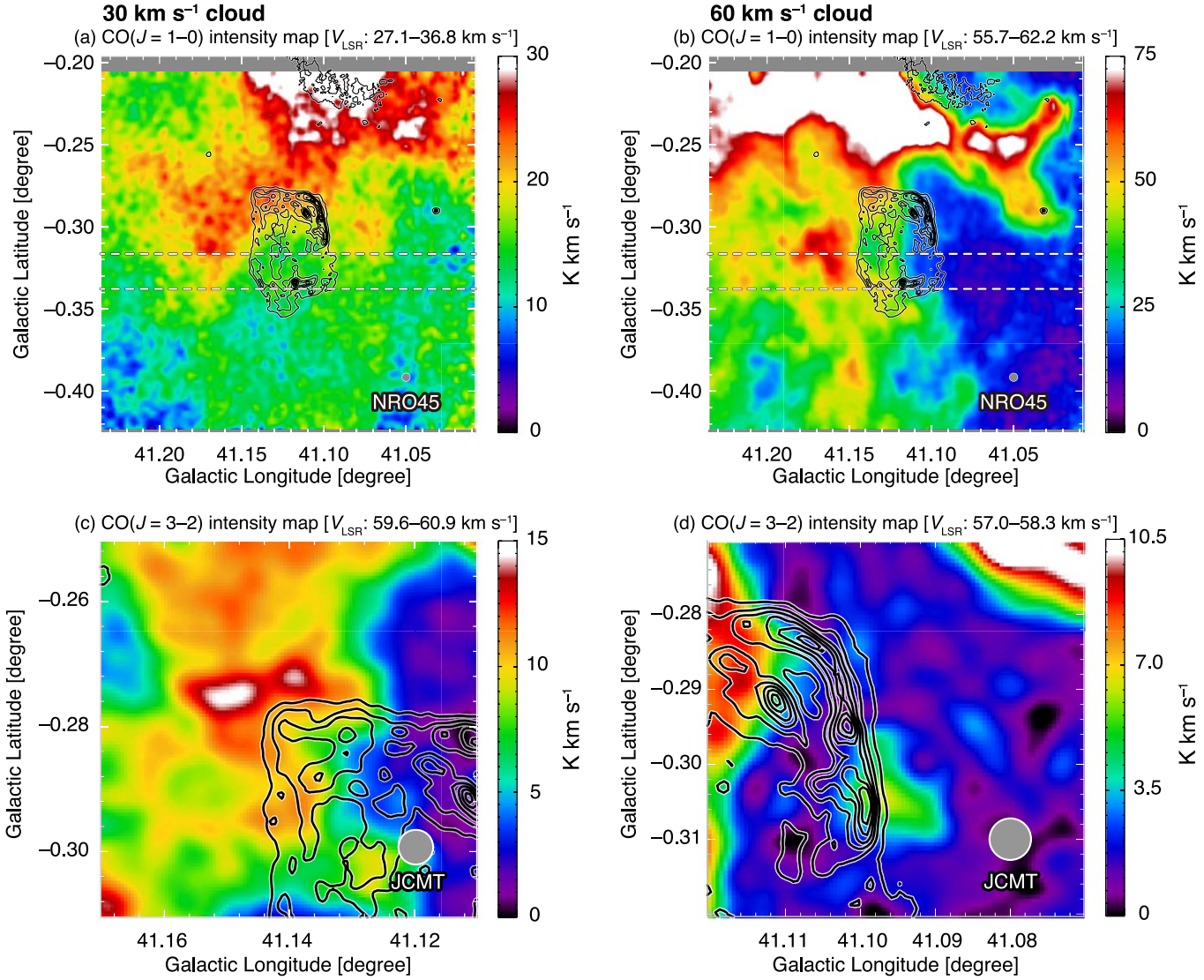

Figure 3. (a) and (b) Integrated intensity maps of NRO45 ^{12}CO(J = 1–0) for (a) the the 30 km s^{-1} cloud and (b) the 60 km s^{-1} cloud. The integration velocity range of 27.1–36.8 km s^{-1} for the 30 km s^{-1} cloud and 55.7–62.2 km s^{-1} for the 60 km s^{-1} cloud. Horizontal dashed lines represent the integration ranges of Galactic latitude for each cloud (see Figure 4). (c) and (d) Enlarged maps of the northwestern and southern shells of the 60 km s^{-1} cloud, which were created by using the archival JCMT ^{12}CO(J = 3–2) data (G. Park et al. 2023). The superposed contours are the same as those shown in Figure 1.

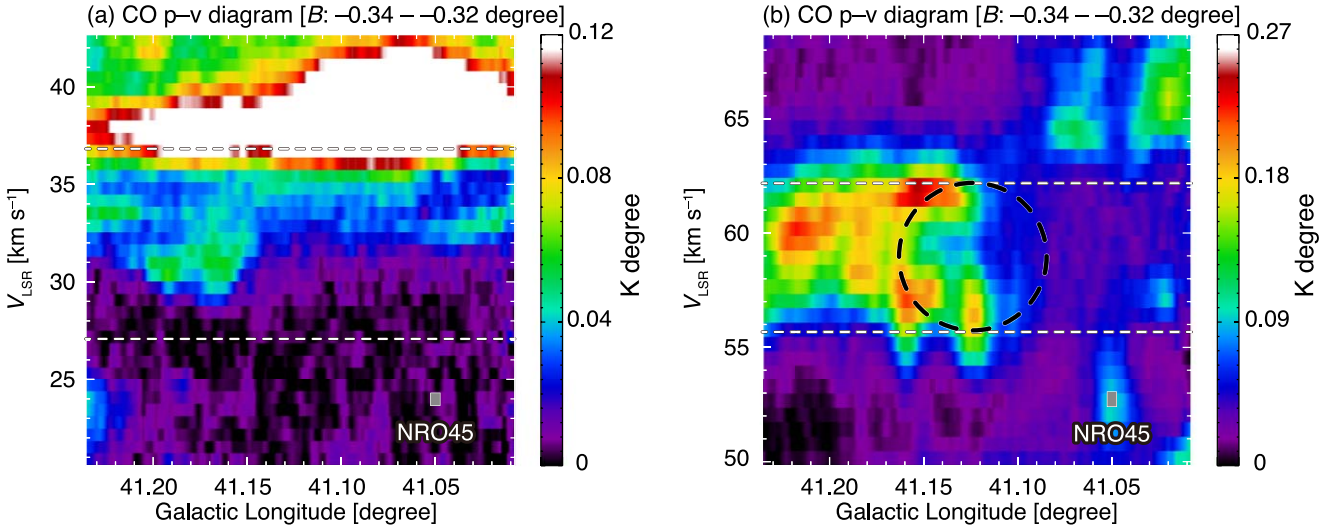

Figure 4. Position–velocity diagrams of NRO45 ^{12}CO(J = 1–0) for (a) the 30 km s^{-1} cloud and (b) the 60 km s^{-1} cloud. The integration range of Galactic longitude is from $-0.^{\circ}34$ to $-0.^{\circ}32$. The dashed circle in (b) indicates an expanding gas motion. Horizontal dashed lines represent the integration velocity ranges for each cloud.

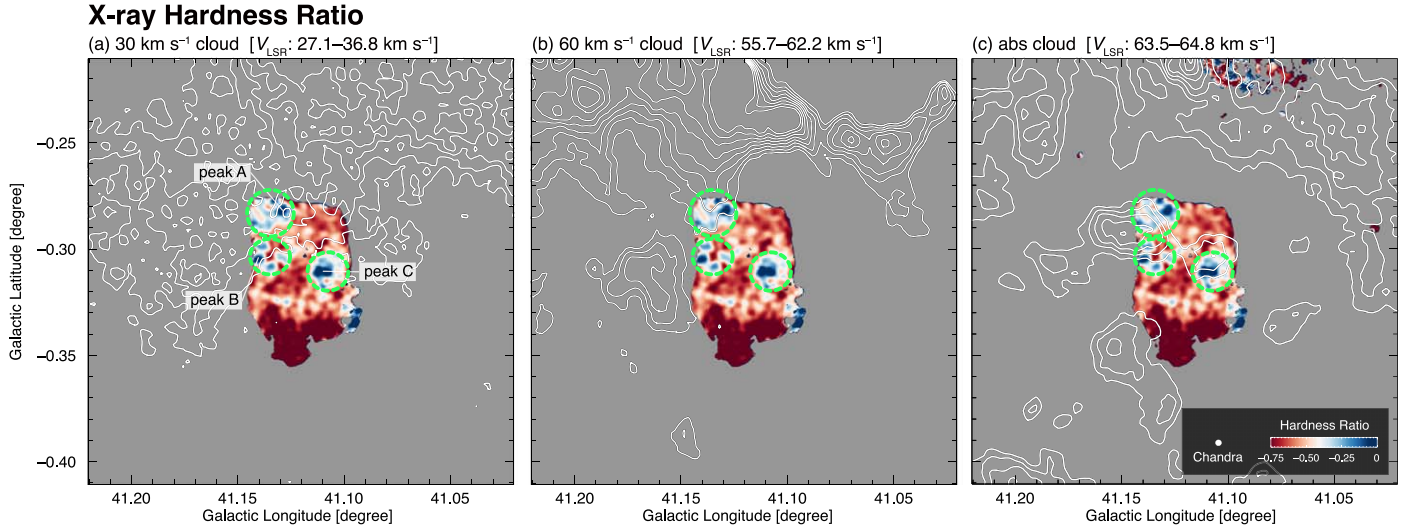

Figure 5. X-ray hardness ratio maps overlaid with the NRO45 ^{12}CO(J = 1–0) contours of (a) the 30 km s^{-1} cloud, (b) the 60 km s^{-1} cloud, and (c) the abs cloud. The energy band of the hardness ratio map is 1.14–1.27 keV for the soft band and 3.3–3.7 keV for the hard band. The shaded areas are excluded because of outside the radio continuum shell. The white contours indicate the ^{12}CO(J = 1–0) integrated intensities, whose lowest contour level and contour intervals are 14.0 and 2.8 K km s^{-1} for the 30 km s^{-1} cloud; 50.0 and 6.0 K km s^{-1} for the 60 km s^{-1} cloud; and 7.5 and 2.0 K km s^{-1} for the abs cloud, respectively. The green dashed circles, named peaks A, B, and C, represent the three regions with relatively higher hardness ratios.

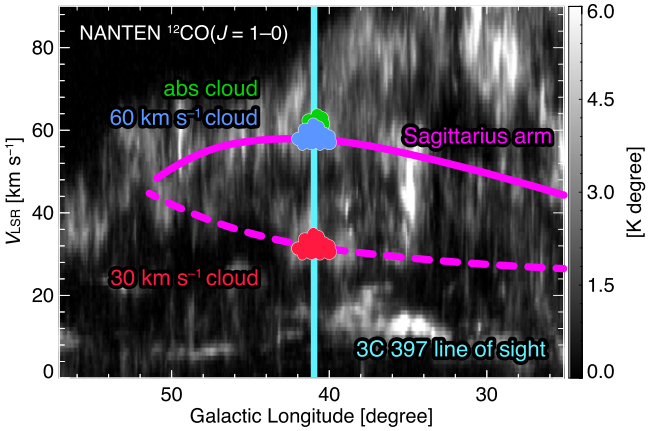

Figure 6. Large-scale position–velocity diagram of ^{12}CO(J = 1–0) obtained with the NANTEN 4 m radio telescope (A. Mizuno & Y. Fukui 2004). The integration range in the Galactic longitude is from −1° to 1°. The dashed and solid curves indicate the near- and farside Sagittarius arms, respectively. The cyan vertical line represents the line-of-sight direction of 3C 397. We also plotted the 30 km s^{-1} cloud (red), abs cloud (green), and 60 km s^{-1} cloud (blue).

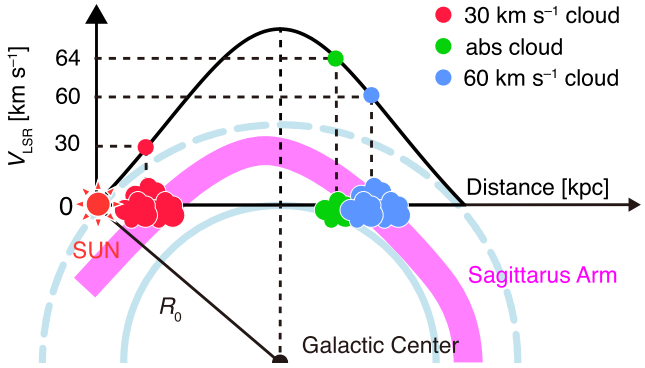

Figure 7. Schematic view of the Galactic spiral arm and the distance–velocity relation. The solid black curve shows the relation between the line-of-sight velocity and kinematic distance. The red, green, and blue clouds represent the 30 km s^{-1} cloud, abs cloud, and 60 km s^{-1} cloud, respectively. The red thick curve indicates the Sagittarius arm. R_0 is the distance from the Galactic center to the Sun.

absorption study) and the positional relation among the molecular clouds and 3C 397 toward the line of sight.

4.2. Age of 3C 397

The previous section suggested that the distance of 3C 397 is slightly updated from ∼10 to ∼8.7 kpc. We here estimated the dynamical age t_{age} of the SNR based on our revised distance of 3C 397. Since the 3C 397 is believed to be in the Sedov–Taylor Phase (L. I. Sedov 1959), we can estimate the dynamical age as below,

$$t_{age} = \frac{2r}{5V_{sh}}, \quad (2)$$

where V_{sh} is the shock velocity of the SNR and $r = 4.04$ pc is the radius of the SNR shell. By adopting the shock velocity $V_{sh} = 1050$–1360 km s^{-1} (D. A. Leahy & S. Ranasinghe 2016), we obtain the SNR age t_{age} = 1100–1400 yr. This value is roughly consistent with the previous age estimation of the 3C 397 that assumed a similar distance (e.g., D. A. Leahy & S. Ranasinghe 2016).

4.3. A Hint for a Single-degenerate Origin

In this section, we discuss whether the expanding gaseous shell of the 60 km s^{-1} cloud was formed before or after the SN explosion of 3C 397, by comparing the physical properties such as the mass of the evacuated gaseous shell and the preshock density. The total mass of the evacuated gaseous shell M could be calculated using the following equations:

$$M = m_p \mu \Omega D^2 \sum_i N_i(\mathrm{H_2}), \quad (3)$$

$$N(\mathrm{H_2}) = X \cdot W(\mathrm{CO}), \quad (4)$$

where m_p is the mass of atomic hydrogen, $\mu = 2.8$ is the mean molecular weight, Ω is the solid angle for each data pixel, D is the distance to the SNR, $N(\mathrm{H_2})$ is the molecular hydrogen column density, and W(CO) is the intensity of the ^{12}CO(J = 1–0).

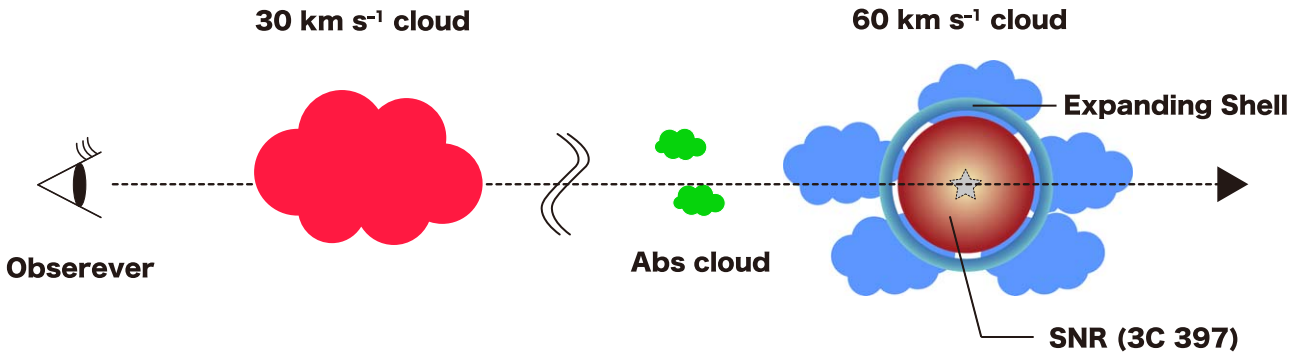

Figure 8. Schematic image of the positional relation between each molecular cloud and 3C 397 in the line-of-sight direction. The red, green, and blue clouds represent the 30 km s^{-1} cloud, abs cloud, and 60 km s^{-1} cloud, respectively.

If the derived mass of the expanding shell was uniformly distributed over the present volume of the remnant before being blown out, the preshock density of the neutral gas is estimated to be $\sim$800 cm^{-3}. On the other hand, D. A. Leahy & S. Ranasinghe (2016) calculated the preshock density of $\sim$2−5 cm^{-3} using the previously derived postshock density from the infrared observation and X-ray emission measure (S. Safi-Harb et al. 2005; H. Yamaguchi et al. 2015).

This discrepancy implies that the expanding gaseous shell in the 60 km s^{-1} cloud likely had been formed before the SN explosion of 3C 397. In other words, the SN explosion of 3C 397 occurred inside a low-density cavity with an expanding velocity of a few km s^{-1}. In the case of a Type Ia progenitor system like 3C 397, the OTW expected in the SD scenario is the most promising way to form such an expanding shell before the SN explosion. In fact, Type Ia SNRs N103B and G344.7–0.1, which can be understood as the same SD scenario, actually have very similar physical quantities to 3C 397 (e.g., mass and expanding velocity of neutral gas; H. Sano et al. 2018; K. Fukushima et al. 2020). Since there are phases in the DD channel that are not yet well understood, this study does not exclude the DD scenario for 3C 397, but it is consistent with the OTW in the SD scenario. A further careful search for a companion star surviving the SN explosion will shed light on distinguishing the SD and DD scenarios.

5. Conclusion

We summarize our conclusions as follows:

(1.) New ^{12}CO($J = 1$–0) observations using the Nobeyama 45 m radio telescope revealed the spatial distributions of two CO clouds at $V_{LSR} = 27.1$–36.8 km s^{-1} (the 30 km s^{-1} cloud) and 55.7–62.2 km s^{-1} (the 60 km s^{-1} cloud) with an unprecedented angular resolution of 18″. We found that both clouds show good spatial correspondence with the radio continuum shell of the SNR. The spatial distributions of archival ^{12}CO($J = 3$–2) data at the $\sim$20″ resolution also show highly excited cloudlets in the 60 km s^{-1} cloud, which are nicely along the edge or boundary of the radio-continuum shell.

(2.) The 60 km s^{-1} cloud shows a cavity-like structure in a position–velocity diagram, the spatial extent of which is roughly consistent with that of the SNR. This cavity-like structure is generally thought to be an expanding gas motion due to the pre- and/or postsupernova feedback, and hence the 60 km s^{-1} cloud has a systemic velocity of $\sim$59 km s^{-1} and an expansion velocity of $\sim$3 km s^{-1}. On the other hand, the 30 km s^{-1} cloud does not show any such characteristic features.

(3.) The CO cloud at V_{LSR} = 62.8–65.4 km s^{-1} (the abs cloud) lies in the regions where the X-ray HR shows higher values. This indicates that the abs cloud is located in front of the SNR because the larger value of the X-ray HR represents the higher photoelectric absorption value toward the line of sight. By considering the distributions of Galactic spiral arms and X-ray HR, the 30 km s^{-1} cloud should be located at the nearside arm and the others lie on the farside arm. The kinematic distance cloud be derived using the Galactic rotation curve model to be $\sim$2.1 kpc for the 30 km s^{-1} cloud, $\sim$8.3 kpc for the abs cloud, and $\sim$8.7 $\pm$ 0.2 kpc for the 60 km s^{-1} cloud. We, therefore, concluded that the 60 km s^{-1} cloud is the one most likely interacting with the SNR.

(4.) The total gaseous mass within the SNR shell was estimated to be $\sim 8.6 \times 10^3 M_\odot$. If all the expanding gas was driven by the SN shock waves, the preshock density was estimated to be $\sim$800 cm^{-3}. Since the preshock density is inconsistent with the previously estimated value of $\sim$2–5 cm^{-3}, 3C 397 likely exploded inside a low-density bubble formed by the OTW. We propose a possible scenario that the progenitor system of 3C 397 is a white dwarf and its companion star, and then an SD explosion occurred.

Acknowledgments

We acknowledge Rin Yamada, Yuto Onishi, Hiroki Teramoto, Maki Aruga, Kohei Matsubara, Yurina Yamanaka, and Koharu Hirano for contributions to the observations and data reductions of ^{12}CO($J = 1$–0) data. The Nobeyama 45 m radio telescope is operated by the Nobeyama Radio Observatory, a branch of the National Astronomical Observatory of Japan. The James Clerk Maxwell Telescope is operated by the East Asian Observatory on behalf of The National Astronomical Observatory of Japan; Academia Sinica Institute of Astronomy and Astrophysics; the Korea Astronomy and Space Science Institute; the National Astronomical Research Institute of Thailand; Center for Astronomical Mega-Science (as well as the National Key R&D Program of China with No. 2017YFA0402700). Additional funding support is provided by the Science and Technology Facilities Council of the United Kingdom and participating universities and organizations in the United Kingdom and Canada. The NANTEN project is based on a mutual agreement between Nagoya University and the

Carnegie Institution of Washington (CIW). We greatly appreciate the hospitality of all the staff members of the Las Campanas Observatory of CIW. We are thankful to many Japanese public donors and companies who contributed to the realization of the project. This paper employs a list of Chandra data sets, obtained by the Chandra X-ray Observatory, contained at doi:10.25574/cdc.187. This research has made use of software provided by the Chandra X-Ray Center in the application package CIAO (v4.14). This work was also supported by JSPS KAKENHI grant Nos. 21H01136 and 24H00246 (HS). This work was supported by a University Research Support Grant from the National Astronomical Observatory of Japan (NAOJ). This work was also supported by NAOJ ALMA Scientific Research Grant Code 2023-25A. This research was partially supported by CCI Holdings Co., Ltd.

Appendix
Radius and Thickness of the Expanding Shell

To derive the radius and thickness of the expanding shell, we fitted the radial profile of the radio continuum surface brightness using a 3D spherical shell with a Gaussian function $F(r)$:

$$F(r) = A \exp\left[-\frac{(r - r_0)^2}{2\sigma^2}\right], \quad \text{(A1)}$$

where r is the radius of the radio continuum shell and σ is the standard deviation of the Gaussian function. We first fitted with a radial profile by moving the origin to determine the geometric center of the SNR. We obtained $(l, b) = (41.^{\circ}03, -0.^{\circ}3)$ as the geometric center with the minimum chi-square value of the least-squares fitting. Figure 9 shows the radial profile of the radio continuum at the center position $(l, b) = (41.^{\circ}03, -0.^{\circ}3)$.

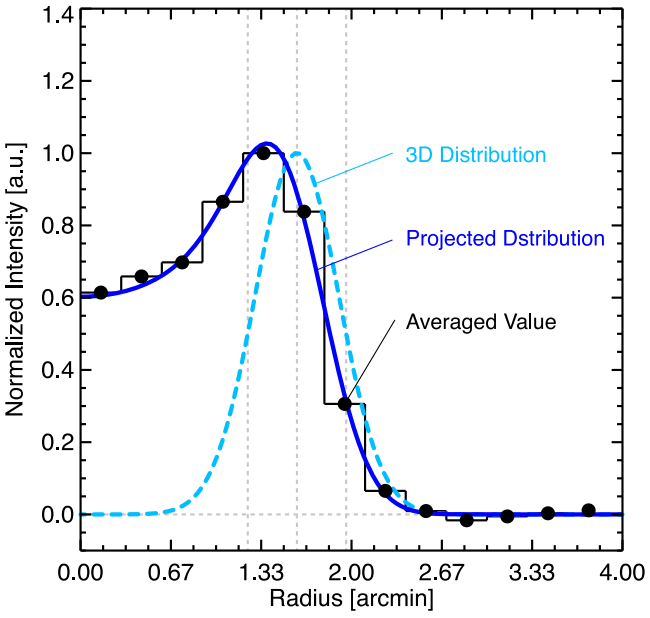

Figure 9. Radial profiles of the radio continuum centered at $(l, b) = (41.^{\circ}12, -0.^{\circ}31)$. The black dots and steps are the averaged values of the radio continuum within each annulus. The dashed and solid curves represent the three-dimensional and projected Gaussian distributions, respectively. These curves were obtained by least-squares fitting. The gray dashed vertical lines represent best-fit values for the shell radius and thickness.

We obtained $r \sim 4.04$ pc ($1.'60$) for the shell radius and $\sigma \sim 1.84$ pc ($0.'73$) for the shell thickness as best-fit values, where the shell thickness is defined by the Gaussian FWHM or $2\sigma\sqrt{2\ln 2}$. In the present paper, we assumed that the size of the gaseous expanding shell is roughly consistent with that of the radio continuum in the SNR (see, H. Sano et al. 2021, 2022; M. Aruga et al. 2022).

ORCID iDs

D. Ito https://orcid.org/0009-0000-4742-5098
H. Sano https://orcid.org/0000-0003-2062-5692
K. Nakazawa https://orcid.org/0000-0003-2930-350X
I. Mitsuishi https://orcid.org/0000-0002-9901-233X
Y. Fukui https://orcid.org/0000-0002-8966-9856

References

Anderson, M. C., & Rudnick, L. 1993, ApJ, 408, 514
Aruga, M., Sano, H., Fukui, Y., et al. 2022, ApJ, 938, 94
Badenes, C., Hughes, J. P., Bravo, E., & Langer, N. 2007, ApJ, 662, 472
Becker, R. H., Markert, T., & Donahue, M. 1985, ApJ, 296, 461
Brand, J., & Blitz, L. 1993, A&A, 275, 67
Ergin, T., Saha, L., Bhattacharjee, P., et al. 2021, MNRAS, 501, 4226
Fruscione, A., McDowell, J. C., Allen, G. E., et al. 2006, Proc. SPIE, 6270, 62701V
Fukushima, K., Yamaguchi, H., Slane, P. O., et al. 2020, ApJ, 897, 62
Graessle, D. E., Evans, I. N., & Glotfelty, K. 2006, Proc. SPIE, 6270, 62701X
Hachisu, I., Kato, M., Kato, T., & Matsumoto, K. 2000, ApJL, 528, L97
Hachisu, I., Kato, M., & Nomoto, K. 1996, ApJL, 470, L97
Hachisu, I., Kato, M., & Nomoto, K. 1999a, ApJ, 522, 487
Hachisu, I., Kato, M., Nomoto, K., & Umeda, H. 1999b, ApJ, 519, 314
Helfand, D. J., Becker, R. H., White, R. L., Fallon, A., & Tuttle, S. 2006, AJ, 131, 2525
Iben, I.J., & Tutukov, A.V. 1984, ApJ, 284, 719
Inoue, T., Yamazaki, R., & Inutsuka, S.I. 2009, ApJ, 695, 825
Inoue, T., Yamazaki, R., Inutsuka, S.I., & Fukui, Y. 2012, ApJ, 744, 71
Jiang, B., Chen, Y., Wang, J., et al. 2010, ApJ, 712, 1147
Kilpatrick, C. D., Bieging, J. H., & Rieke, G. H. 2016, ApJ, 816, 1
Koo, B.-C., Lee, J.-J., Jeong, I.-G., Seok, J. Y., & Kim, H.-J. 2016, ApJ, 821, 20
Koo, B.-C., & McKee, C. F. 1992a, ApJ, 388, 93
Koo, B.-C., & McKee, C. F. 1992b, ApJ, 388, 103
Koo, B.-C., Reach, W. T., Heiles, C., Fesen, R. A., & Shull, J. M. 1990, ApJ, 364, 178
Kuno, N., Takano, S., Iono, D., et al. 2011, in XXXth URSI General Assembly and Scientific Symp. (Piscataway, NJ: IEEE), 1
Leahy, D. A., & Ranasinghe, S. 2016, ApJ, 817, 74
Lee, Y.-H., Koo, B.-C., Lee, J.-J., Burton, M. G., & Ryder, S. 2019, AJ, 157, 123
Maeda, K., & Terada, Y. 2016, IJMPD, 25, 1630024
Maoz, D., Mannucci, F., & Nelemans, G. 2014, ARA&A, 52, 107
Minamidani, T., Nishimura, A., & Miyamoto, Y. 2016, Proc. SPIE, 9914, 99141Z
Mizuno, A., & Fukui, Y. 2004, in ASP Conf. Ser. 317, Milky Way Surveys: The Structure and Evolution of our Galaxy, 317, ed. D. Clemens, R. Shah, & T. Brainerd (San Francisco, CA: ASP), 59
Nomoto, K. 1982, ApJ, 253, 798
Nomoto, K., Thielemann, F. K., & Yokoi, K. 1984, ApJ, 286, 644
Ohshiro, Y., Yamaguchi, H., Leung, S.-C., et al. 2021, ApJL, 913, L34
Park, G., Currie, M. J., Thomas, H. S., et al. 2023, ApJS, 264, 16
Phillips, M. M. 1993, ApJL, 413, L105
Phillips, M. M., Lira, P., Suntzeff, N. B., et al. 1999, AJ, 118, 1766
Pskovskii, I. P. 1977, SvA, 21, 675
Reid, M. J., Dame, T. M., Menten, K. M., & Brunthaler, A. 2016, ApJ, 823, 77
Rho, J., & Petre, R. 1998, ApJL, 503, L167
Safi-Harb, S., Dubner, G., Petre, R., Holt, S. S., & Durouchoux, P. 2005, ApJ, 618, 321
Safi-Harb, S., Petre, R., Arnaud, K. A., et al. 2000, ApJ, 545, 922
Sano, H., Sato, J., Horachi, H., et al. 2010, ApJ, 724, 59
Sano, H., Suzuki, H., Nobukawa, K. K., et al. 2021, ApJ, 923, 15

Sano, H., Tanaka, T., Torii, K., et al. 2013, ApJ, 778, 59
Sano, H., Yamaguchi, H., Aruga, M., et al. 2022, ApJ, 933, 157
Sano, H., Yamane, Y., Tokuda, K., et al. 2018, ApJ, 867, 7
Sedov, L. I. 1959, Similarity and Dimensional Methods in Mechanics (New York: Academic)
Seta, M., Hasegawa, T., Dame, T. M., et al. 1998, ApJ, 505, 286
Seta, M., Hasegawa, T., Sakamoto, S., et al. 2004, AJ, 127, 1098
Umemoto, T., Minamidani, T., Kuno, N., et al. 2017, PASJ, 69, 78
Weaver, R., McCray, R., Castor, J., Shapiro, P., & Moore, R. 1977, ApJ, 218, 377
Webbink, R. F. 1984, ApJ, 277, 355
Whelan, J., & Iben, I., J. 1973, ApJ, 186, 1007
Yamaguchi, H., Badenes, C., Foster, A. R., et al. 2015, ApJL, 801, L31
Yeung, P. K. H., Bamba, A., & Sano, H. 2023, PASJ, 75, 384
Zhou, P., Chen, Y., & Zhang, Z.Y. 2016, ApJ, 826, 34